JOURNAL OF SPACECRAFT AND ROCKETS
Vol. 44, No. 1, January–February 2007

Multidisciplinary Design Optimization of Space Plane Considering Rigid Body Characteristics

Nobuhiro Yokoyama, Shinji Suzuki,[†] and Takeshi Tsuchiya[‡]
University of Tokyo, Bunkyo-ku, Tokyo 113-8656, Japan
Hideyuki Taguchi[§]
Japan Aerospace Exploration Agency, Mitaka, Tokyo 181-0015, Japan
and
Takeshi Kanda[¶]
Japan Aerospace Exploration Agency, Kakuda, Miyagi 981-1525, Japan

DOI: 10.2514/1.19969

Multidisciplinary design optimization is an important approach for the conceptual design of space planes because these planes are characterized by disciplines that interact with one another. A multidisciplinary design optimization problem of a single-stage-to-orbit space plane is formulated and solved in this study. The modeling and optimization of rigid body characteristics, such as trim and stability, are focused on because a single-stage-to-orbit space plane has a tendency for considerable shift of both the aerodynamic center and the center of gravity. Moreover, the design of the air-breathing engines are integrated with the airframe and its effect on the rigid body characteristics are also modeled in the framework of multidisciplinary design optimization. Using the all-at-once-based multidisciplinary design optimization approach, which incorporates sparse nonlinear programming and metamodeling, the design of the vehicle and its flight trajectory are successfully optimized. Finally, the characteristics of the optimal solution are investigated, especially the relationships among the airframe-engine integration, rigid body characteristics, and payload transportation capability.

Nomenclature

C_D	=	drag coefficient
C_L	=	lift coefficient
C_m	=	pitching moment coefficient acting on the reference point
$C^{\mathrm{ex}}_{m\alpha}$	=	stability index contributed by external nozzle of dual-mode engines
c_w	=	root chord length of the wing
D	=	drag
$\boldsymbol{d}_i$	=	inputs of sample data
$\tilde{\boldsymbol{d}}_i$	=	inputs of test data
e_{mse}	=	mean squared error of metamodel evaluated on the sample points
$F(\boldsymbol{y})$	=	output of metamodel
$\tilde{F}_i$	=	output of test data
$\bar{F}$	=	mean of the output of test data
$\boldsymbol{f}$	=	right-hand side of state equations
G	=	fidelity criterion of the constructed metamodel
g_0	=	acceleration of gravity at sea level (=9.80655 m/s^2)
H	=	altitude
h_e	=	height of the dual-mode engines
I_{sp_D}	=	specific impulse of the dual-mode engines excluding the external nozzle
I_{sp_R}	=	specific impulse of the rocket engines
I_{yy}	=	moment of inertia with respect to the pitch axis
J	=	objective function
L	=	lift
l_b	=	total body length
l_n	=	forebody length
l_e	=	x-coordinate of the leading edge of the dual-mode engines
l_w	=	x-coordinate of the leading edge of the wing root
M	=	flight Mach number
M_A	=	aerodynamic pitching moment with respect to the center of gravity
M_D	=	pitching moment with respect to the center of gravity produced by T_D
M^{ex}_D	=	pitching moment with respect to the center of gravity produced by T^{ex}_D and N^{ex}_D
M_R	=	pitching moment with respect to the center of gravity produced by T_R
M_{ref}	=	aerodynamic pitching moment acting on the reference point
m	=	number of phases
$\tilde{m}$	=	mass of the vehicle
$\tilde{m}_E$	=	estimated total mass of the vehicle excluding the payload mass
$\tilde{m}^f_{\mathrm{LH2}}$	=	mass of the consumed liquid hydrogen in the forward tanks
$\tilde{m}^r_{\mathrm{LH2}}$	=	mass of the consumed liquid hydrogen in the rear tanks
$\tilde{m}_{\mathrm{LOX}}$	=	mass of the consumed liquid oxygen
$\tilde{m}_{\mathrm{PAY}}$	=	payload mass
$\tilde{m}_{\mathrm{TO}}$	=	takeoff mass of the vehicle
N^{ex}_D	=	normal force (perpendicular to the thrust) of the dual-mode engines acting on the external nozzle
n_c	=	number of selected sample points ($n_c \leq n_s$)
n_j	=	number of segments in jth phase

Presented as Paper 710 at the 43rd AIAA Aerospace Sciences Meeting and Exhibit, Reno, Nevada, 10–13 January 2005; received 9 September 2005; revision received 13 June 2006; accepted for publication 15 July 2006. Copyright © 2006 by the American Institute of Aeronautics and Astronautics, Inc. All rights reserved. Copies of this paper may be made for personal or internal use, on condition that the copier pay the $10.00 per-copy fee to the Copyright Clearance Center, Inc., 222 Rosewood Drive, Danvers, MA 01923; include the code $10.00 in correspondence with the CCC.

*Research Associate, Operation and Safety Technology Team, 6-13-1 Osawa, Mitaka; currently Japan Aerospace Exploration Agency. Member AIAA.

[†]Professor, Department of Aeronautics and Astronautics, 7-3-1 Hongo, Bunkyo-ku. Senior Member AIAA.

[‡]Associate Professor, Department of Aeronautics and Astronautics, 7-3-1 Hongo, Bunkyo-ku. Member AIAA.

[§]Associate Senior Researcher, Supersonic Transport Team, 6-13-1 Osawa, Mitaka. Member AIAA.

[¶]Manager, Combined Propulsion Research Group, 1 Koganesawa, Kimigaya, Kakuda. Senior Member AIAA.

n_s = number of sample points
n_t = number of test points (not for cross-validation)
P_D = internal pressure of the dual-mode engines
p = dimension of the input to metamodel
Q = pitch rate
q = flight dynamic pressure
r = geocentric distance
$\boldsymbol{S}$ = static variables
s_{ex} = area of the external nozzle projected on the body axis
T_D = thrust of the dual-mode engines excluding the external nozzle
T_D^{ex} = thrust of the dual-mode engines acting on the external nozzle
T_R = thrust of the rocket engines
$T_{R\max}$ = maximum thrust of the rocket engines
t = time
$\boldsymbol{U}$ = control variables
V = velocity
w_b = body width
w_f = width of the nose
$(x_{\mathrm{ref}}, z_{\mathrm{ref}})$ = position of the aerodynamic reference point
(x_D, z_D) = point of action with respect to T_D
$(x_D^{\mathrm{ex}}, z_D^{\mathrm{ex}})$ = point of action with respect to T_D^{ex} and N_D^{ex}
(x_R, z_R) = point of action with respect to T_R
$(x_{\mathrm{CG}}, z_{\mathrm{CG}})$ = position of the vehicle's center of gravity
$\boldsymbol{X}$ = state variables
$\boldsymbol{y}$ = input of metamodel
α = angle of attack
β = radius of the Gaussian function
γ = flight path angle
δ_e = elevon deflection angle
δ_R = thrust angle of rocket engines
ε = proportion of liquid hydrogen consumption in the forward tanks
ζ = inequality path constraint functions
$\boldsymbol{\eta}$ = equality constraint functions for static variables
θ_b = inclination angle of the external nozzle
θ_f = inclination angle of the precompression surface of the forebody
$\boldsymbol{\kappa}$ = inequality constraint functions for static variables
Λ = swept angle of the wing
λ = taper ratio of the wing
μ = gravitational constant of the earth ($=3.986 \times 10^{14}\ \mathrm{m^3/s^2}$)
ν = liquid hydrogen/liquid oxygen mixture ratio of rocket engines ($=6.0$)
ξ = weight parameters of the radial basis functions network metamodel
ρ = weighting parameter of constrained subuniform design
$\boldsymbol{\sigma}$ = equality path constraint functions
$\boldsymbol{\varphi}, \tilde{\boldsymbol{\varphi}}$ = functions to express the continuity of the variables between adjacent phases
$\boldsymbol{\chi}_0$ = inequality functions for the initial conditions for a phase
$\boldsymbol{\chi}_f$ = inequality functions for the terminal conditions for a phase
$\boldsymbol{\psi}_0$ = equality functions for the initial conditions for a phase
$\boldsymbol{\psi}_f$ = equality functions for the terminal conditions for a phase
ω = angular velocity of the rotation of the earth ($=7.277 \times 10^{-5}\ \mathrm{rad/s}$)

I. Introduction

TO promote space exploration in the future, it is necessary to develop a low-cost and highly reliable space transportation system. In particular, single-stage-to-orbit (SSTO) space planes may be a promising concept for such a potential system due to their reusability, system simplicity (e.g., no separation mechanism), and operational flexibility for takeoff and landing. However, unlike multiple stage vehicles, the feasibility of an SSTO vehicle is severely limited because it must be placed on the low-earth orbit (LEO) without separation of heavy components that are unnecessary for the orbital or reentry flight. Thus, the optimization approach to maximize the payload weight plays an important role in the conceptual design of an SSTO vehicle. On the other hand, the design of a space plane involves multiple disciplines (e.g., trajectory, aerodynamics, structure, propulsion, etc.) that interact with one another [1–3]. This fact indicates that an independent design optimization in each discipline does not necessarily lead to a desirable design for the entire system. Therefore, multidisciplinary design optimization (MDO) techniques, which integrate the simulation tools of constituent disciplines and optimize the entire system, have offered a great advantage to the conceptual design of space planes [1,2,4].

It is desirable that the analysis model of each discipline be sufficiently accurate and reliable to obtain a practical result obtained through MDO. In view of flight dynamics, it is important to model the rigid body characteristics such as trim and stability. In particular, space planes have a tendency for considerable shift of both the aerodynamic center (AC) and the center of gravity (CG) as they accelerate from takeoff velocity to orbital velocity. These shifts can cause severe instability and produce large moments that must be counteracted. Furthermore, the design requires that the air-breathing engines be integrated with the airframe to improve the propulsion performance [5], which substantially affects the rigid body characteristics of the space plane. For example, the lift acting on the external nozzle due to combustion gas can produce an excessive nose-down moment that cannot be counteracted. However, in previous MDO studies of SSTO, a simulation model that covers both the rigid body characteristics, i.e., trim and stability, as well as the engine-airframe integration has rarely been researched. In [3], a multidisciplinary parametric analysis covering the trim was performed, however, the application was limited to a rocket-powered vertical takeoff SSTO vehicle. In our past work [6], MDO was applied to a horizontal takeoff SSTO vehicle powered by air-breathing engines and rocket engines (RE), but the effect of the integration of the air-breathing engine with the airframe was not investigated. Therefore, this study formulates and solves an MDO problem by considering the engine-airframe integration and its effect on rigid body characteristics such as trim and stability.

Although there are several advanced MDO methods such as individual disciplinary feasible method [7], collaborative optimization [2], and bilevel integrated system synthesis [8], this study adopts the all-at-once (AAO) method [9] incorporating some useful techniques. In the AAO method, all the nonlinear equations in the MDO problem are solved simultaneously without the inner iteration of each analysis program, which often deteriorates the robustness and rate of convergence. In addition, the convergence of the AAO method is not affected by the coupling between multiple disciplines unlike those of the other MDO methods. Thus, the AAO method has the advantages that the robustness and rate of convergence are generally better than those of the other approaches [9]. However, it is difficult to embed complicated analysis programs into the framework of the AAO method. To circumvent this difficulty, metamodels (mathematical approximation models of the relationships between the inputs and outputs of original analyses) are constructed externally and then used in the framework of the AAO method. The other difficulty in the AAO method is that the resulting nonlinear programming (NLP) problem tends to be large. We applied a sparse nonlinear programming technique to reduce the computational time for solving the resulting large NLP problem. Using the AAO-based MDO incorporating these two techniques, the conceptual design of the vehicle and its flight trajectory are successfully optimized. Moreover, the characteristics of the optimal solution, especially the relationships among the airframe-engine integration, rigid body characteristics, and payload transportation capability, are investigated.

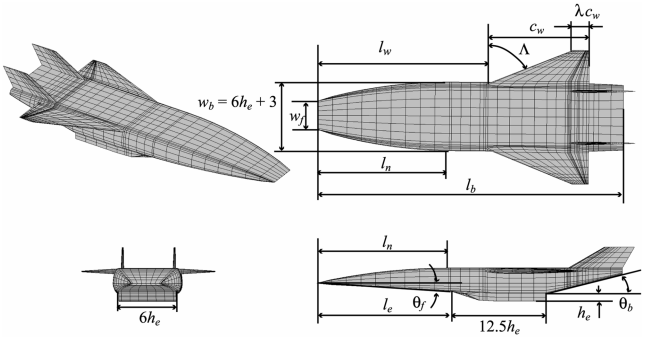

Fig. 1 Basic configuration and shape design variables.

II. Analysis Models

The analysis models used in the MDO framework are described in the following subsections.

A. Definition of System Configuration, Mission, and Objective Function

Figure 1 shows the basic airframe configuration of the vehicle as well as the shape design variables to be optimized. As can be seen in Fig. 1, a planular airframe is adopted so as to attain a favorable propulsion performance. The maximum height above the body axis is fixed to 2 m. The wing section is NACA0005. The elevons comprise 25% of the wing chord and 90% of the exposed wing semispan. The total area of the two vertical tails is 13% of the wing area. As the air-breathing engine, a variable-geometry dual-mode engine (DME) [10], which can be operated in the ramjet and scramjet modes, is integrated with the bottom side of the airframe [11]. In addition, RE is mounted on the base side of the airframe. The propellants are liquid hydrogen, LH_2, and liquid oxygen, LOX. It should be noted that the LH_2 tanks are located separately in the front and rear of the LOX tank. Thus, the LH_2 tanks are used as the trim tanks. The cross-sectional area of the tanks at every section is constrained within 50% of the cross-sectional area of the fuselage. The length and location of each tank are also among the design variables to be optimized. The constraints imposed on the shape design are shown in Table 1.

The mission is specified as follows:

1) The vehicle takes off from the runway propelled by the RE.

2) The vehicle accelerates and ascends with the sequential operation of the propulsion system as follows: RE $\rightarrow$ DME+ RE $\rightarrow$ DME $\rightarrow$ DME + RE $\rightarrow$ RE.

3) At an altitude above 90 km, the RE is cut off and the vehicle begins coasting.

4) At the altitude of 100 km, which is the altitude of the target LEO, the RE is reignited to accelerate the vehicle to the orbital velocity.

The takeoff mass of the vehicle is 500 Mg. The goal of the optimization is to maximize the payload mass, which is expressed as follows.

$$\tilde{m}_{\mathrm{PAY}} = \tilde{m}_{\mathrm{TO}} - \tilde{m}_E \tag{1}$$

Thus, the objective function to be minimized is expressed as $J = -\tilde{m}_{\mathrm{PAY}}$.

Table 1 Constraints imposed on the shape design

Inequality constraints	Inequality constraints
$60 \le l_b \le 80$ m	$0.1 \le \lambda \le 0.4$
$3 \le \theta_f \le 8$ deg	$0.2(w_b - 3) \le w_f \le 0.5(w_b - 3)$, m
$10 \le \theta_b \le 20$ deg	$200 \le$ wing exposed area ≤ 1000 m^2
$45 \le \Lambda \le 60$ deg	$2000 \le$ body volume ≤ 8000 m^3
$15 \le c_w \le 25$ m	$l_n \le l_e \le l_w + c_w$
$0.1l_b \le l_n \le 0.5l_b$	external nozzle length ≥ 10 m
$0.1l_b \le l_e \le 0.5l_b$	$l_w + c_w \ge 0.8l_b$
$l_n \le l_w \le l_b - c_w$	$\theta_f \le \tan^{-1}[(w_b - w_f - 3)/(2l_n)] \le 12$ deg
$1.5 \le h_e \le 2.5$ m	——

Table 2 Representative values of the flight condition parameters for aerodynamic analysis

Parameters	Representative values
$\tilde{M}$	0.2, 0.7, 0.9, 1.05, 1.2, 3.8, 8.3, 12.8, 18.0, 23.0, 28.0
(α, δ_e), deg	(0, 0), (5, 0), (10, 0), (5, −10), (5, 10)

B. Aerodynamics

The lift coefficient, drag coefficient, and pitching moment coefficient are calculated based on combinations of the representative values of the flight Mach number, angle of attack, and elevon deflection angle, as shown in Table 2.

The linear potential flows are calculated by the panel method [12] at $\tilde{M} \le 1.2$. The Prandtl–Meyer expansion flow theory and the tangent cone method [13] are applied at $\tilde{M} \ge 3.8$. The skin friction drag is estimated by the van Driest method [14] and the base drag is estimated by an empirical equation of the aerodynamic preliminary analysis system [15]. Moreover, the aerodynamic characteristics at the representative $\tilde{M}$ of the transonic regime (i.e., $\tilde{M} = 1.05$) are assumed to be the same as those at $\tilde{M} = 1.2$. When the DME is not operated, its inlet and exit are assumed to be closed. Under this condition, the pressure coefficient at the backward-facing step flow region, i.e., at the closed-exit and a part of the external nozzle, is calculated based on experimental and empirical equations [15,16]. The reattachment length of the backward-facing step flow is specified as $7h_e$ for a subsonic flow [17] and $3h_e$ for a supersonic flow [18]. Moreover, as shown in Fig. 2, virtual panels are introduced to calculate a reasonable potential flow at $\tilde{M} \le 1.2$.

Given the shape of the vehicle, the aerodynamic coefficients at the representative values are calculated, and they are given in the following second order polynomials of α and δ_e.

$$\begin{aligned} C_L &= C_{L0} + C_{L1}\alpha + C_{L2}\alpha^2 + C_{L3}\delta_e + C_{L4}\delta_e^2 \\ C_D &= C_{D0} + C_{D1}\alpha + C_{D2}\alpha^2 + C_{D3}\delta_e + C_{D4}\delta_e^2 \\ C_m &= C_{m0} + C_{m1}\alpha + C_{m2}\alpha^2 + C_{m3}\delta_e + C_{m4}\delta_e^2 \end{aligned} \tag{2}$$

The parameters $C_{L0}, \ldots, C_{L4}, C_{D0}, \ldots, C_{D4}, C_{m0}, \ldots, C_{m4}$ are given as the functions of $\tilde{M}$ by interpolating the data obtained from the analysis. This modeling of the aerodynamic coefficients supports the contribution of the incidental force produced by the elevon deflection (e.g., trim drag).

The analysis methods used in this study are less accurate than the recent computational fluid dynamics (CFD) approaches that solve the Euler or Navier–Stokes equations; nevertheless, they have the following advantages:

1) It is relatively easy to implement a program for automatic generation of the grid required for the aerodynamic calculations.

2) The computational costs for the applied methods are moderate, whereas those for the recent CFD approaches are usually high.

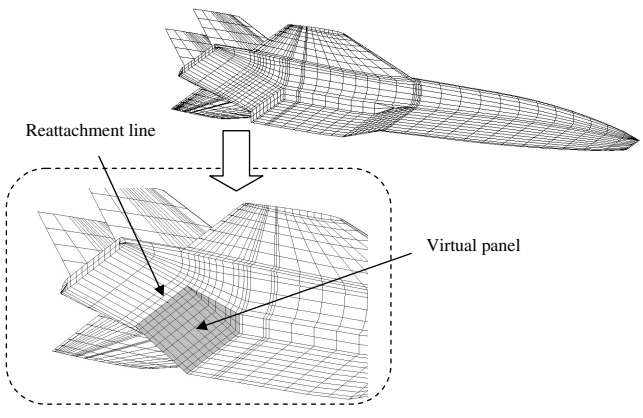

Fig. 2 Virtual panel for potential flow calculation.

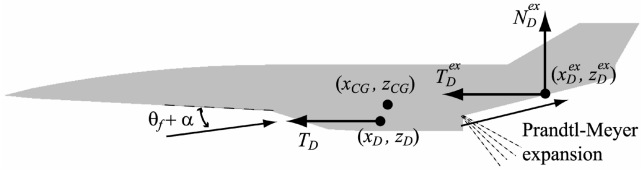

Fig. 3 Forces generated by DME and their action points.

However, these methods still consume considerable computational time if they are directly applied in the framework of MDO. Therefore, metamodels of the parameters $C_{L0}, \ldots, C_{L4}$, $C_{D0}, \ldots, C_{D4}$, $C_{m0}, \ldots, C_{m4}$ were constructed.

C. Propulsion System

The number of DME is specified as six, and its possible operating Mach number is assumed to be from $\tilde{M} = 3.8$ to $\tilde{M} = 12.8$. The design variables related to the DME are the total projected area of the DME (i.e., $6h_e^2$), the inclination angle of the precompression surface, the x-coordinate of the leading edge of the engine, and the inclination angle of the external nozzle, as shown in Fig. 1. It should be noted that the performance of the DME can be enhanced further via rigorous design optimization of its configuration, however, it is not performed in this study for simplicity. The thrust coefficient and the specific impulse of the DME, excluding the effect of the external nozzle, are given as the functions of the flight Mach number, the altitude, and the airflow angle at the inlet. In addition, the combustion gas properties (static pressure, static temperature, Mach number, ratio of specific heat, and molecular mass) at the exit of the DME and its internal pressure are given as functions of $\tilde{M}$, H, and $(\theta_f + \alpha)$. On the basis of the combustion gas properties at the exit, the thrust, the normal force, and the action point of the pitching moment at the external nozzle are calculated. The Prandtl–Meyer theory is used to calculate the pressure of the expansion flow, and the friction coefficient is specified as 0.002. Figure 3 is a schematic view of the forces generated by the DME and their action points. On the other hand, the maximum internal pressure of the DME is used to estimate its weight, as explained in Sec. II.E. All the functions of $\tilde{M}$, H, and $(\theta_f + \alpha)$ as described are approximated by the metamodels for their application in the MDO framework.

The number of RE is specified as 10. The thrust and the specific impulse of the RE are given as functions of the altitude. The vacuum thrust of the RE is a design variable, and the vacuum specific impulse is specified as 455.2 s.

D. Trajectory and Flight Dynamics

An ascent trajectory optimization problem is considered. For simplicity, the motion of the vehicle is constrained on the equatorial plane and only the longitudinal dynamics are covered. The motion of the vehicle is controlled by δ_e, T_R, and δ_R. Furthermore, as mentioned in Sec. II.A, it is assumed that it is possible to control the proportion of LH_2 consumption at the forward and rear tanks. The motion of the vehicle, which takes the rigid body dynamics into account, is defined by the following set of differential equations.

$$\frac{d\tilde{m}^f_{\mathrm{LH2}}}{dt} = \left(\frac{T_D}{I_{\mathrm{sp}_D}} + \frac{1}{1+\nu}\frac{T_R}{I_{\mathrm{sp}_R}}\right)\frac{\varepsilon}{g_0} \tag{3}$$

$$\frac{d\tilde{m}^r_{\mathrm{LH2}}}{dt} = \left(\frac{T_D}{I_{\mathrm{sp}_D}} + \frac{1}{1+\nu}\frac{T_R}{I_{\mathrm{sp}_R}}\right)\frac{1-\varepsilon}{g_0} \tag{4}$$

$$\frac{d\tilde{m}_{\mathrm{LOX}}}{dt} = \left(\frac{\nu}{1+\nu}\frac{T_R}{I_{\mathrm{sp}_R}}\right)\frac{1}{g_0} \tag{5}$$

$$\frac{dr}{dt}\left(=\frac{dH}{dt}\right) = V\sin\gamma \tag{6}$$

$$\frac{dV}{dt} = \frac{(T_D + T_D^{\mathrm{ex}})\cos\alpha + T_R\cos(\alpha+\delta_R) - D - N_D^{\mathrm{ex}}\sin\alpha}{\tilde{m}} + \left(r\omega^2 - \frac{\mu}{r^2}\right)\sin\gamma \tag{7}$$

$$\frac{d\gamma}{dt} = \frac{L + N_D^{\mathrm{ex}}\cos\alpha + (T_D + T_D^{\mathrm{ex}})\sin\alpha + T_R\sin(\alpha+\delta_R)}{\tilde{m}V} + \frac{1}{V}\left(\frac{v^2}{r} + r\omega^2 - \frac{\mu}{r^2}\right)\cos\gamma + 2\omega \tag{8}$$

$$\frac{d\alpha}{dt} = -\frac{d\gamma}{dt} + Q \tag{9}$$

$$\frac{dQ}{dt} = \frac{M_A + M_D + M_D^{\mathrm{ex}} + M_R}{I_{yy}} \tag{10}$$

where

$$\tilde{m} = \tilde{m}_{\mathrm{TO}} - (\tilde{m}^f_{\mathrm{LH2}} + \tilde{m}^r_{\mathrm{LH2}} + \tilde{m}_{\mathrm{LOX}}) \tag{11}$$

$$M_A = M_{\mathrm{ref}} - (L\cos\alpha + D\sin\alpha)(x_{\mathrm{ref}} - x_{\mathrm{CG}}) - (L\sin\alpha - D\cos\alpha)(z_{\mathrm{ref}} - z_{\mathrm{CG}}) \tag{12}$$

$$M_D = -T_D(z_D - z_{\mathrm{CG}}) - T_D^{\mathrm{ex}}\left(z_D^{\mathrm{ex}} - z_{\mathrm{CG}}\right) - N_D^{\mathrm{ex}}\left(x_D^{\mathrm{ex}} - x_{\mathrm{CG}}\right) \tag{13}$$

$$M_D^{\mathrm{ex}} = -T_D^{\mathrm{ex}}(z_D^{\mathrm{ex}} - z_{\mathrm{CG}}) - N_D^{\mathrm{ex}}(x_D^{\mathrm{ex}} - x_{\mathrm{CG}}) \tag{14}$$

$$M_R = -T_R\sin\delta_R(x_R - x_{\mathrm{CG}}) - T_R\cos\delta_R(z_R - z_{\mathrm{CG}}) \tag{15}$$

The state equations (3–10) tend to be a stiff system because the time scale of the pitch rate is considerably smaller than those of the other state variables. The stiffness of the system often makes it difficult to solve the trajectory optimization problem; this is because the resulting matrix in the NLP problem is often ill-conditioned. Therefore, it is assumed that the pitch rate is settled at any time of the flight, i.e., $\dot{Q} = 0$, and it is also assumed that any angle of attack can be attained instantly by the control system. The state equations are then converted to differential algebraic equations (DAE) composed of Eqs. (3–8) and the following equation.

$$M_A + M_D + M_D^{\mathrm{ex}} + M_R = 0 \tag{16}$$

Equation (16) actually represents the static trim condition. The converted DAE are relatively easy to solve due to relieved stiffness, and the contributions of the original dynamics [Eq. (10)] to the flight performances are approximately covered by Eq. (16).

The liftoff velocity and the total ground-roll distance are restrained within 150 m/s and 3000 m, respectively. The takeoff performance is calculated by the analytical method given in [19], where the maximum value of C_L is supposed to be the C_L at $\alpha = 15$ deg and $\delta_e =$ trim angle.

The control variables of the trajectory optimization are constrained as follows.

$$\begin{aligned} &0 \le \alpha \le 15\,\text{deg}: \text{DME is not operated} \\ &0 \le \alpha \le 12 - \theta_f\,\text{deg}: \text{DME is operated} \end{aligned} \tag{17}$$

$$\left.\begin{aligned} T_R &= 0 \\ \delta_R &= 0 \end{aligned}\right\}: \text{RE is not operated}$$
$$\left.\begin{aligned} 0.2T_{R\max} \le T_R &\le T_{R\max} \\ -15 \le \delta_R &\le 15\,\text{deg} \end{aligned}\right\}: \text{RE is operated} \tag{18}$$

$$\left.\begin{aligned} -10 \le \delta_e &\le 10\,\text{deg} \\ 0 \le \varepsilon &\le 1 \end{aligned}\right\}: \text{Throughout the flight} \tag{19}$$

It should be noted that the angle of attack is actually bound by the other control variables in the equality condition (16). Moreover, the time history of ε is actually bound by the volume of the forward and rear LH_2 tanks. Throughout the flight, the following variables are constrained to be less than their designed maximum values: the thrust of the DME, internal pressure of the DME, flight dynamic pressure, load factor, and axial acceleration (i.e., acceleration with respect to the body axis).

With regard to the reentry flight, the flight dynamics and the trajectory are not directly optimized, however, the flight corridor appropriate for the equilibrium glide is considered by imposing constraints on the aeroheating, load factor, and dynamic pressure.

Furthermore, the aerodynamic stability condition is defined as the inequality

$$\frac{\partial(M_A + M_D + M_D^{\text{ex}} + M_R)}{\partial\alpha} = \frac{\partial(M_A + M_D + M_D^{\text{ex}})}{\partial\alpha} \le 0 \tag{20}$$

where M_R is not affected by the angle of attack.

E. Weight Estimation

The design variables of the vehicle's structure are the maximum flight dynamic pressure, maximum load factor, maximum axial acceleration, maximum thrust of the DME, and maximum internal pressure of the DME. These design variables are optimized in the MDO framework. The weight of the components, except for the propulsion system, are estimated by hypersonic aerospace sizing analysis (HASA) [20] and some modifications were made to the original HASA. It is assumed that the structural weight can be reduced to 50% of the aluminum-based structural weight if a considerable part of the structure is made of advanced materials such as C/C. This is because the specific tensile strength of C/C [21] is more than twice that of an aluminum alloy. Thus, the coefficient 0.5 is multiplied with the structural weight equations in the original HASA. The avionics weight is also reduced to 69% of the weight in the original HASA. This is based on the assumption that the advanced avionics system [22], which is lighter than the current system, is used. In addition, the propellant tanks are regarded as integral tanks and their weights are assumed to be included in the body weight. The weight of the DME is calculated by a structural analysis and is given as a function of the maximum internal pressure and projected cross-sectional area, where the material of its structure is assumed to be SiC/SiC. The variable structure of the DME is calculated by weights analysis of advanced transportation systems [23]. With respect to the RE, the thrust-to-weight ratio is specified as 60.0.

On the basis of the weights and locations of components, the position of the vehicle's CG at dry condition is calculated. Then the vehicle's CG at any flight condition is calculated in the trajectory analysis. For simplicity, the CG positions of the forward/rear LH_2 and LOX are assumed to be the same as those of the tanks, regardless of the filling rates.

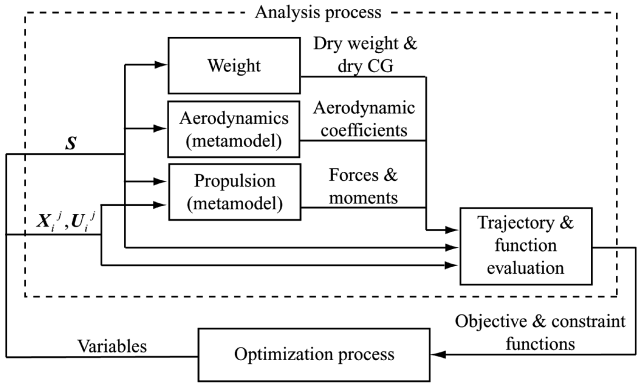

Fig. 4 Schematic view of AAO-based MDO framework.

III. MDO Framework

Integrating each disciplinary analysis in the previous section, the AAO-based MDO framework is constructed as shown in Fig. 4. The framework is an extended form of the direct (NLP-based) trajectory optimization, in which the vehicle design optimization problem (i.e., weight, aerodynamics, and propulsion) is embedded. In addition, all the nonlinear equations in the analysis are treated as parts of the constraints or objective function and are simultaneously solved in the optimization process. Because the aerodynamic analysis and propulsion analysis are complicated, their metamodels are constructed externally and then embedded in the MDO framework. On the other hand, the weight analysis does not employ metamodels, because it is simple and does not include inner iterative process. Although each of the disciplinary models described in the preceding section have sufficient accuracy for the conceptual design, more accurate numerical codes can be applied in the MDO framework if they are sufficiently approximated by the metamodels. Thus, the presented MDO framework can be applied to a wide range of problems.

The following subsections describe two important aspects of the MDO framework: the construction method of the metamodels and the formulation of the NLP problem.

A. Construction of Metamodels

Among the available candidates for the metamodel, such as polynomials and Kriging [24], the radial basis functions network (RBFN) [25] is employed as the metamodel in this study. The RBFN has the following advantages:

1) Fitting algorithms and validation methodologies are substantially simpler than those used for the Kriging model because, like polynomials, the RBFN is a linear combination of bases.

2) It can approximate any type of multi-input nonlinear function; this is generally difficult with polynomials.

Let us denote the inputs and the output as $\boldsymbol{y}(\in \mathbb{R}^p)$ and $F(\boldsymbol{y})(\in \mathbb{R})$, respectively. The RBFN metamodel used in this study is then expressed as the linear combination of the Gaussian

$$F(\boldsymbol{y}) = \sum_{i=1}^{nc} \xi_i \prod_{j=1}^{p} \exp[-(y_j - d_{ij})^2/\beta_j^2] \tag{21}$$

where ξ_i $(1 \le i \le n_c)$ are the weight parameters, $\boldsymbol{d}_i = [\,d_{i1} \quad d_{i2} \cdots d_{ip}]^T$ $(i = 1, \ldots, n_c)$ are the centers of the Gaussian (selected from sample input points), and β_j $(j = 1, \ldots, p)$ are the radii of the Gaussian. The weight parameters and the centers of the Gaussian are determined by the orthogonal least squares (OLS) algorithm [26] under the sample data (input-output relationship), the values of β_j, and the allowable mean squared error (MSE) of the sample data. To attain a robust approximation performance, β_j $(j = 1, \ldots, p)$ and e_{mse} are optimized on the basis of cross validation, in which additional sample data (not included in the n_s sample set) are prepared and the MSE of these additional samples is used as the performance index to evaluate the robustness of the approximation.

The simulated annealing (SA) algorithm supporting the continuous variables [27] is used to obtain the optimal β_j $(j = 1, \ldots, p)$ and e_{mse} that minimize the MSE of the additional sample data.

The arrangement of the sample inputs is referred to as experimental design. Because the input dimension of the propulsion metamodels is three [i.e., $\tilde{M}$, H, and $(\theta_f + \alpha)$], which is low enough, the grid-based experimental design was adopted. On the other hand, because the input dimension of the aerodynamic metamodels is 11 (i.e., the number of shape design variables), which is relatively high, it is computationally prohibitive to adopt the grid-based experimental design as n_s is exponential to the input dimension. Considering the constrained design space of the vehicle's shape as shown in Table 1, we adopted an efficient experimental design referred to as constrained subuniform design (CSUD) [28] for the construction of the aerodynamic metamodels. In the design space that is irregularly shaped by many constraints, the CSUD arranges the inputs approximately uniformly in terms of Euclidian space and arranges each input axis by maximizing the following performance index.

$$\sum_{i=1}^{n_s} \log\Big(\min_{1\le j(\neq i)\le n_s} \|\boldsymbol{d}_i - \boldsymbol{d}_j\|\Big) + \rho \sum_{i=1}^{n_s}\sum_{k=1}^{p} \log\Big(\min_{1\le j(\neq i)\le n_s} |d_{ik} - d_{jk}|\Big) \tag{22}$$

where $\|\ \|$ denotes the Euclidian norm and d_{ik}, d_{jk} denote the kth component of vector $\boldsymbol{d}_i$, $\boldsymbol{d}_j$ respectively. The SA algorithm is used to explore the optimum of this problem. The CSUD is similar to the Latin hypercube design incorporating the maximin design [29], however, its advantage is that the accuracy of the metamodels can be enhanced by covering only the reasonable design space that is irregularly shaped by the constraints. The aerodynamic metamodels were constructed by preparing 200 data sampled by the CSUD and 200 additional data for cross validation sampled by the Monte Carlo method on each representative value of $\tilde{M}$, (α, δ_e) shown in Table 2.

The fidelity of the constructed metamodels was checked by the following criterion.

$$G = \sum_{i=1}^{n_t} [F(\tilde{\boldsymbol{d}}_i) - \tilde{F}_i]^2 \Big/ \sum_{i=1}^{n_t} (\tilde{F}_i - \bar{F})^2 \tag{23}$$

This criterion means the normalized MSE at another test data (not used for cross validation) arranged by the Monte Carlo method, and ranges from zero to one. The larger G becomes, the more accurate the constructed metamodel. The worst (the smallest) G value of propulsion metamodels was more than 0.99, which is large enough. On the other hand, the average and worst G value of aerodynamic metamodels were 0.985 and 0.775, respectively. These values indicate that the errors of the aerodynamic metamodels may not be neglected. Consequently, a two-stage MDO approach as described in the next section was used to eliminate the influence of the approximation errors of the aerodynamic metamodels on the solutions.

B. Formulation of the AAO-based NLP Problem

The trajectory optimization problem embedded with the design optimization problem is formulated in an NLP problem. To convert the trajectory optimization problem into an NLP problem, direct collocation [30] is applied. The formulation of the NLP is outlined as follows.

By dividing the flight sequence into m phases, we discretize the time domain $[t_0^j, t_f^j]$ of each phase j to $(n_j + 1)$ nodes as $t_0^j, t_1^j, \ldots, t_{nj}^j (= t_f^j)$. Note that the phase corresponds to the operation mode of propulsion system (e.g., DME mode, RE mode, etc.). Express the state and control variables as $\boldsymbol{X}_i^j$, $\boldsymbol{U}_i^j$ $(i = 1, \ldots, n_j, j = 1, \ldots, m)$, where the superscript and the subscript correspond to a phase and a node, respectively. The state variables $\boldsymbol{X}_i^j$ include r, V, γ, $\tilde{m}_{\text{LH2}}^f$, $\tilde{m}_{\text{LH2}}^r$, and $\tilde{m}_{\text{LOX}}$, and the control variables $\boldsymbol{U}_i^j$ include α, δ_e, δ_R, T_R, and ε. The elements of $\boldsymbol{S}$ include the unknown terminal time t_f^j and the design variables of the vehicle (e.g., shape design variables, the maximum values of engines thrust, the maximum dynamic pressure, and so on). Adopting the optimization variables as $\boldsymbol{X}_i^j$, $\boldsymbol{U}_i^j$ $(i = 1, \ldots, n_j, j = 1, \ldots, m)$, and $\boldsymbol{S}$, the NLP problem is formulated as follows.

1) Objective function:

$$\text{minimize} \qquad J(\boldsymbol{X}_{nm}^m, \boldsymbol{U}_{nm}^m, \boldsymbol{S}) \tag{24}$$

As mentioned before, the objective function is defined as $J = -\tilde{m}_{\text{PAY}}$, and $\tilde{m}_{\text{PAY}}$ is computed from the total propellant weight (the function of $\boldsymbol{X}_{nm}^m$) and the dry weight of the vehicle (the function of $\boldsymbol{S}$).

2) Initial conditions of phase j at time $t = t_0^j$

$$\left.\begin{aligned} \boldsymbol{\psi}_0^j(\boldsymbol{X}_0^j, \boldsymbol{U}_0^j, \boldsymbol{S}) &= 0 \\ \boldsymbol{\chi}_0^j(\boldsymbol{X}_0^j, \boldsymbol{U}_0^j, \boldsymbol{S}) &\ge 0 \end{aligned}\right\} \qquad (j = 1, \ldots, m) \tag{25}$$

These constraints denote the takeoff conditions including the liftoff velocity and the total ground-roll distance as described previously.

3) Connection conditions between phase j and phase $j + 1$ at time $t = t_0^{j+1} (= t_f^j)$

$$\phi^{j+1}(\boldsymbol{X}_0^{j+1}, \boldsymbol{U}_0^{j+1}, \boldsymbol{S}) - \tilde{\phi}^j(\boldsymbol{X}_{nj}^j, \boldsymbol{U}_{nj}^j, \boldsymbol{S}) = 0 \qquad (j = 1, \ldots, m-1) \tag{26}$$

This condition enforces the continuity of all the state variables and some of the control variables (i.e., α, δ_e, ε).

4) Equality constraints for the implicit integration of the state equations (separated Hermite–Simpson scheme [30])

$$\left.\begin{aligned} \boldsymbol{X}_{i+1}^j - \frac{\boldsymbol{X}_{i+2}^j + \boldsymbol{X}_i^j}{2} - \frac{\boldsymbol{f}^j(\boldsymbol{X}_i^j, \boldsymbol{U}_i^j, \boldsymbol{S}) - \boldsymbol{f}^j(\boldsymbol{X}_{i+2}^j, \boldsymbol{U}_{i+2}^j, \boldsymbol{S})}{8}(t_{i+2}^j - t_i^j) &= 0 \\ \boldsymbol{X}_{i+2}^j - \boldsymbol{X}_i^j - \frac{\boldsymbol{f}^j(\boldsymbol{X}_i^j, \boldsymbol{U}_i^j, \boldsymbol{S}) + 4\boldsymbol{f}^j(\boldsymbol{X}_{i+1}^j, \boldsymbol{U}_{i+1}^j, \boldsymbol{S}) + \boldsymbol{f}^j(\boldsymbol{X}_{i+2}^j, \boldsymbol{U}_{i+2}^j, \boldsymbol{p})}{6}(t_{i+2}^j - t_i^j) &= 0 \end{aligned}\right\}$$
$$(i = 0, 2, \ldots, 2n_j - 2, \quad j = 1, \ldots, m) \tag{27}$$

where $\boldsymbol{f}$ corresponds to the right-hand side of the state equations (3–8).

5) Path constraints

$$\left.\begin{aligned} \boldsymbol{\sigma}^j(\boldsymbol{X}_i^j, \boldsymbol{U}_i^j, \boldsymbol{S}) &= 0 \\ \boldsymbol{\zeta}^j(\boldsymbol{X}_i^j, \boldsymbol{U}_i^j, \boldsymbol{S}) &\ge 0 \end{aligned}\right\} \qquad (i = 0, \ldots, n_j, \quad j = 1, \ldots, m) \tag{28}$$

These constraints correspond to Eqs. (16–20) as well as the constraints on the thrust of the DME, internal pressure of the DME, flight dynamic pressure, load factor, and axial acceleration.

6) Terminal conditions of phase j at time $t = t_f^j$

$$\left.\begin{aligned} \boldsymbol{\psi}_f^j(\boldsymbol{X}_{nj}^j, \boldsymbol{U}_{nj}^j, \boldsymbol{S}) &= \boldsymbol{0} \\ \boldsymbol{\chi}_f^j(\boldsymbol{X}_{nj}^j, \boldsymbol{U}_{nj}^j, \boldsymbol{S}) &\ge \boldsymbol{0} \end{aligned}\right\} \qquad (j = 1, \ldots, m) \tag{29}$$

These conditions include the constraint on the operating Mach number at each propulsion mode and the constraints to put the vehicle on the target LEO.

7) Constraints on the static variables

$$\left.\begin{aligned} \boldsymbol{\eta}(\boldsymbol{S}) &= 0 \\ \boldsymbol{\kappa}(\boldsymbol{S}) &\ge 0 \end{aligned}\right\} \tag{30}$$

These conditions include all the constraints on the vehicle design (e.g., the constraints shown in Table 1, constraints for the tank position and length to carry propellants, constraints for engine mounting, etc.).

It is known that the convergence of the direct collocation is substantially robust [30] unlike the trajectory optimization based on an explicit integration scheme [31]. On the other hand, its disadvantage is that the resulting NLP problem has a large number of variables and constraints. Nevertheless, the Jacobian of the constraints and the Hessian of the Lagrangian become sparse matrices, as shown in Fig. 5. Thus, a novel sparse sequential

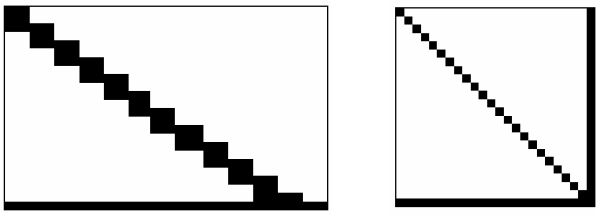

a) b)

Fig. 5 Sparse patterns of a) Jacobian of constraints, and b) Hessian of Lagrangian.

quadratic programming (sparse SQP) code [32], which exploits the sparsity of these matrices, is used to solve the NLP problem. This substantially reduces the computational time as compared with conventional NLP methods.

IV. Results and Discussion

Three cases were considered with respect to the trim and the stability conditions.

Case 1 (unconstrained case): Both the trim (16) and stability (20) conditions were neglected. Alternatively, the conditions $\delta_e = \delta_R = 0$ and $\varepsilon = 0.5$ were imposed. The resulting state equation describes the point mass dynamics.

Case 2 (trim-constrained case): The trim condition (16) was imposed, but the stability condition (20) was neglected.

Case 3 (trim- and stability-constrained case): The stability condition (20) was imposed until the termination of the DME operation; it was neglected thereafter. On the other hand, the trim condition (16) was imposed throughout the ascent flight.

In each case, the total number of nodes with respect to the trajectory integration was specified as 505. The initial guess of the trajectory at the DME operation phase was fixed to the maximum dynamic pressure of 100 kPa, which has been a typical choice for space planes with air-breathing engines. The trim as well as the stability was neglected in the initial guess. The initial guess of the other trajectory profiles and the design variables of the vehicle were arbitrarily determined. To eliminate the influence of the approximation errors of the aerodynamic metamodels on the solution in each case, we used a two-stage MDO in the following manner. First, the regular MDO, which has the same framework as described in the preceding section, was carried out. Using the shape design variables obtained through the regular MDO, the original aerodynamic analysis (not using metamodel) was subsequently carried out. Then, the secondary MDO, which fixes the shape design variables to the values obtained by the regular MDO and the aerodynamic coefficients to the values obtained by the original aerodynamic analysis, was carried out. Note that the secondary MDO does not employ the aerodynamic metamodel, and it optimizes the variables except for the shape design variables.

The optimal solution in this study was defined as the mathematical local optimum whose residual (infinity norm) of the Karush–Kuhn–Tucker equations [30] is less than 10^{-9}, where the objective function and the constraint functions are normalized such that the 2-norm of their gradients become 1.0 at the initial guess. In each MDO, the optimal solution which satisfies the preceding condition was successfully obtained. Using a computer equipped with Intel Xeon 2.8 GHz, the computational time in each MDO was on the tens of minute time scale, whereas the data sampling for the construction of the aerodynamic metamodel took more than 150 h. Thus, most of the computational cost was taken by the construction of metamodels, and computational cost for optimization was much lower. The low computational cost of the optimizations is mainly due to the efficiency of the sparse SQP code. The feature of the AAO method with metamodels, namely, no inner iterations in each disciplinary analysis and function smoothness, may also contribute to the robust and fast convergence of the optimization.

Tables 3 and 4 and Fig. 6 show the specifications and the shapes of the optimal solutions as well as the initial guess. In Tables 3 and 4, the payload weight is not included in the dry weight (the weight of the airframe excluding that of the engines). Under the weight estimation model used in this study, all the optimal solutions achieved payload transportation capability (i.e., positive value of $\tilde{m}_{\mathrm{PAY}}$), although this was not achieved in the initial guess. In addition, the payload weight decreased as the conditions on the trim and stability were enforced. In particular, the payload weight decreased substantially in case 3. Because of the smaller external nozzle, as can be seen in case 3 of Fig. 6, the total thrust coefficient and the specific impulse of the DME are smaller than those in the other optimal solutions. This is the prime reason for the decrease in the payload weight in case 3.

As can be seen in Fig. 6, the wing is located rearward in cases 2 and 3 so as to increase the effect of the elevon deflection and to satisfy the trim condition. However, the trailing edge of the wing does not coordinate with that of the fuselage in both the cases. This is because of the necessity to alleviate the nose-down moment of the wing at the DME operation phase, at which the external nozzle additionally produces the nose-down moment.

It can be seen that the total projected area of the DME in each optimal solution became smaller than those in the initial guess, and this resulted in a reduction in the weight of the DME. On the other hand, all the optimal solutions have a larger θ_f than the initial guess to capture a larger amount of airflow at the inlet. Thus, all the optimal solutions attained larger thrust coefficients of the DME. However, as the conditions on the trim and stability were enforced, the optimal θ_f decreased. This may be relevant to the body volume and the position of the DME in each solution. In other words, in case the DME is located forward of the body, the increase in the body volume due to the large value of θ_f is substantially restrained, hence the increase in the structural weight can be avoided. In addition, the optimal shape in case 3 has a larger wing and larger value of l_n as compared with the other two optimal solutions. It is known that these two features (i.e., shrinking forebody and large delta wing) contribute to stability enhancement. As can be seen in Table 3, $l_e = l_n$ holds in all the optimal solutions. (Note that the constraint $l_n \leq l_e$ was imposed as shown in Table 1.) Thus, to shape the shrinking forebody, the DME was located relatively rearward in case 3. Moreover, the solutions in cases 1 and 2 had minimum base area to equip the RE so as to reduce the base drag, and the tendency of base area reduction can also be observed in case 3 in view of its large θ_b.

The following features can also be seen in Table 3.

1) The flight time for case 1 was long because the range of the Mach number of the DME operation was wide as compared with the other cases.

2) The effect of the wide-range operation of the DME in case 1 appeared in the smaller total propellant weight as compared with the other cases.

3) The RE in case 3 was large due to the necessity of assisting the trim by the thrust vector of the RE.

Figure 7 shows the time histories of the altitude in all the cases. Figures 8 and 9 show the history of the altitude and the flight dynamic pressure with respect to the flight Mach number in all the cases. The common features of the optimal solutions are as follows.

1) The flight dynamic pressure increased after takeoff, and it decreased at the transonic regime to reduce the increase in the drag.

2) As the Mach number approached the starting Mach number of the DME operation (i.e., $\tilde{M} = 3.8$), the vehicle dived to attain a large dynamic pressure as can be seen in Fig. 8, which is favorable for the propulsion performance of the DME. The vehicle turned immediately after the operation of the DME to reduce the drag.

During the operation of the DME, it was observed that on some occasions during flight, the flight dynamic pressure detached its maximum value in the optimal solutions. The reason for this can be explained by Fig. 10, which shows the flight dynamic pressure, the thrust of the DME, and the internal pressure of the DME in case 3. As can be seen in Fig. 10, when q was not bound by its maximum value, T_D or P_D was bound by its maximum value during a considerable portion of the DME operation. The same tendencies were observed in cases 1 and 2 as well. The larger the maximum values assumed by q, T_D, and P_D, the heavier is the structural weight of the airframe and the

Table 3 Specifications of the initial guess and the optimal solutions

Parameters	Initial	Case 1	Case 2	Case 3
Payload weight, Mg	−7.464	14.50	11.71	2.499
Dry weight, Mg	86.60	68.66	63.09	72.52
Airframe weight, Mg	62.11	55.38	49.88	54.66
DME weight, Mg	17.69	8.145	7.816	9.926
RE weight, Mg	6.798	5.138	5.393	7.939
LH_2 weight, Mg	100.6	109.4	89.77	103.3
LOX weight, Mg	312.9	300.3	329.0	315.2
Reentry fuel weight, Mg	7.398	7.104	6.390	6.408
Mach number at				
RE → DME + RE	3.800	3.800	3.800	3.800
DME + RE → DME	5.000	4.199	5.929	5.286
DME → DME + RE	11.00	11.40	10.27	10.22
DME + RE → RE	12.00	12.65	11.83	11.41
Flight time, s	850.2	2183	1468	1347
Maximum value of				
Dynamic pressure, kPa	100.0	43.41	40.91	78.59
Load factor	2.500	2.500	2.500	2.500
Axial acceleration	2.500	1.645	1.780	2.198
Thrust of DME, MN	2.500	0.6230	0.6109	1.336
Internal pressure of DME, MPa	3.000	1.021	1.325	1.471
Vacuum thrust of RE, MN	4.000	3.023	3.173	4.671
Total projected area of DME, m^2	37.50	23.27	20.56	23.85
l_b, m	70.00	65.08	60.82	62.71
l_e, m	28.00	15.87	18.64	27.34
l_n, m	26.60	15.87	18.64	27.34
l_w, m	41.90	29.67	38.50	35.20
w_b, m	18.00	14.82	14.11	14.96
w_f, m	9.750	7.623	6.721	6.922
c_w, m	23.00	22.39	18.49	22.27
Λ, deg	60.00	60.00	58.42	60.00
λ	0.2250	0.1567	0.2191	0.1893
h_e, m	2.500	1.969	1.851	1.994
θ_f, deg	3.000	7.524	6.708	5.265
θ_b, deg	13.00	11.15	14.01	20.00
Body volume, m^3	4094	3839	3298	3716
Front edge position of forward LH_2 tank, m	5.610	5.000	5.000	5.000
Tail edge position of forward LH_2 tank, m	33.75	30.28	40.38	21.80
Front edge position of LOX tank, m	36.17	30.78	40.88	22.30
Tail edge position of LOX tank, m	43.51	37.10	48.69	30.63
Front edge position of rear LH_2 tank, m	45.03	37.60	49.19	31.13
Tail edge position of rear LH_2 tank, m	63.42	61.83	57.78	59.57

weight of the DME. Therefore, the optimal trajectory appeared to be determined on the basis of the tradeoff between the propulsion performance and the structural weight penalty.

On the other hand, in case 3 of Fig. 9, there is a drop in q at around $\tilde{M} = 9.0$, where T_D and P_D are not bound by its maximum value as can be seen in Fig. 10. This can be explained by the profile of $\partial(M_A + M_D + M_D^{\text{ex}})/\partial\alpha$ in case 3, as shown in Fig. 11. In other words, the flight was bound by the stability condition (20) at around $\tilde{M} = 9.0$. The histories of $\partial M_A/\partial\alpha$, $\partial M_D/\partial\alpha$, and $\partial M_D^{\text{ex}}/\partial\alpha$ are also shown in Fig. 11. As can be seen, the inherent stability of the airframe $\partial M_A/\partial\alpha$ was not sustained throughout the DME operation, however, the total stability $\partial(M_A + M_D + M_D^{\text{ex}})/\partial\alpha$ was sustained due to the stability enhancement effect by the external nozzle $\partial M_D^{\text{ex}}/\partial\alpha$. This effect results from the characteristic that the larger the inlet flow angle $(\theta_f + \alpha)$, the higher is the pressure of the combustion gas.

We now define an index $C_{m\alpha}^{\text{ex}}$ as

$$C_{m\alpha}^{\text{ex}} = \frac{1}{q l_b s_{\text{ex}}} \left(\frac{\partial M_D^{\text{ex}}}{\partial \alpha} \right) \tag{31}$$

where $s_{\text{ex}} = 6h_e(l_b - l_e - 12.5h_e)$. The value of $C_{m\alpha}^{\text{ex}}$ can be used as the index of the specific stability enhancement effect by the external

Table 4 Breakdown of airframe dry weight

Component	Initial	Case 1	Case 2	Case 3
Fuselage, Mg	16.93	12.72	11.11	12.71
Wing, Mg	7.467	7.033	5.368	6.556
Tail, Mg	2.293	1.887	1.386	1.878
Gear, Mg	12.85	12.85	12.85	12.85
Thrust structure of DME , Mg	0.812	0.214	0.210	0.441
Thrust structure of RE, Mg	0.5099	0.3853	0.4045	0.5954
Reaction control/orbital maneuvering system, Mg	2.919	3.045	2.738	2.746
Thermal protection system, Mg	7.431	6.676	5.329	6.277
Hydraulics, Mg	0.4035	0.2868	0.2409	0.3424
Avionics, Mg	3.153	3.153	3.153	3.153
Electronics, Mg	2.164	2.125	2.089	2.105
Equipment, Mg	5.000	5.000	5.000	5.000
Total airframe dry weight, Mg	62.12	55.38	49.88	54.65

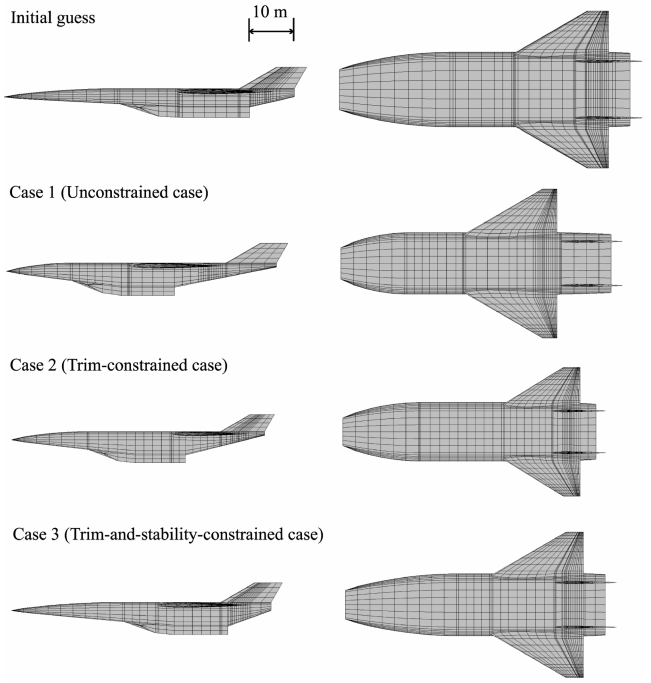

Fig. 6 Shapes of the vehicles.

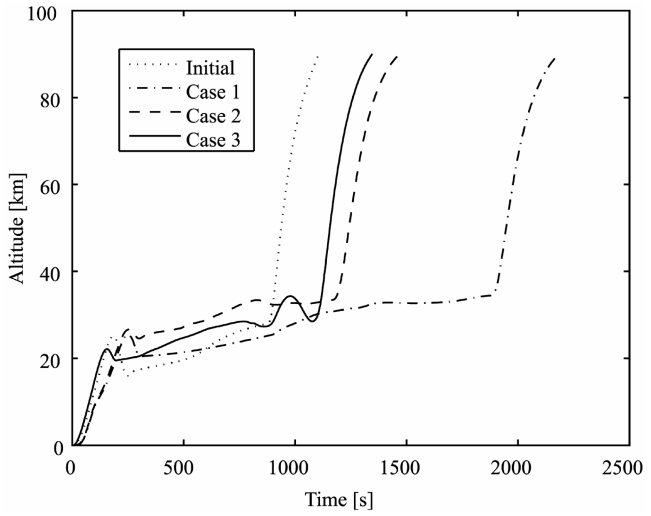

Fig. 7 Time histories of the altitude.

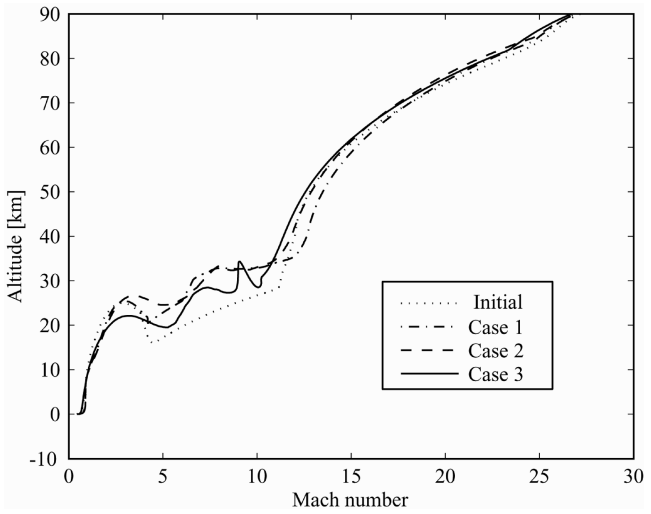

Fig. 8 Histories of the altitude with respect to the flight Mach number.

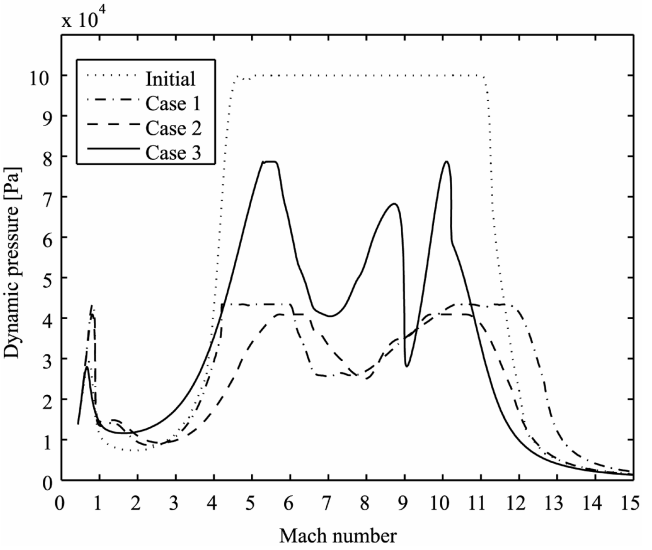

Fig. 9 Histories of flight dynamic pressure with respect to flight Mach number.

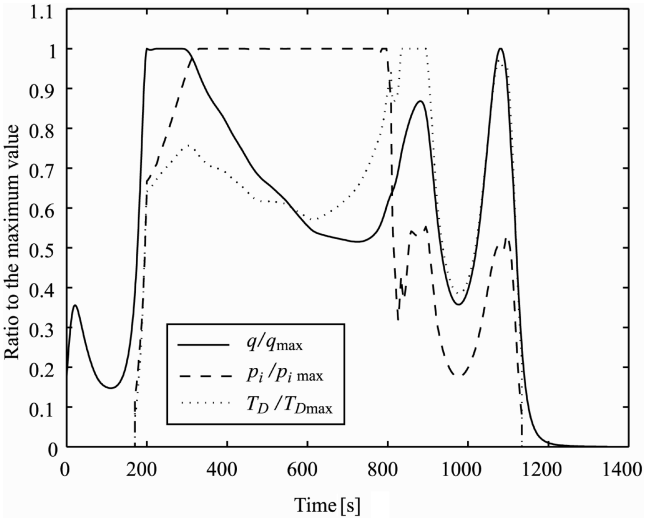

Fig. 10 Time histories of dynamic pressure, thrust, and internal pressure (case 3).

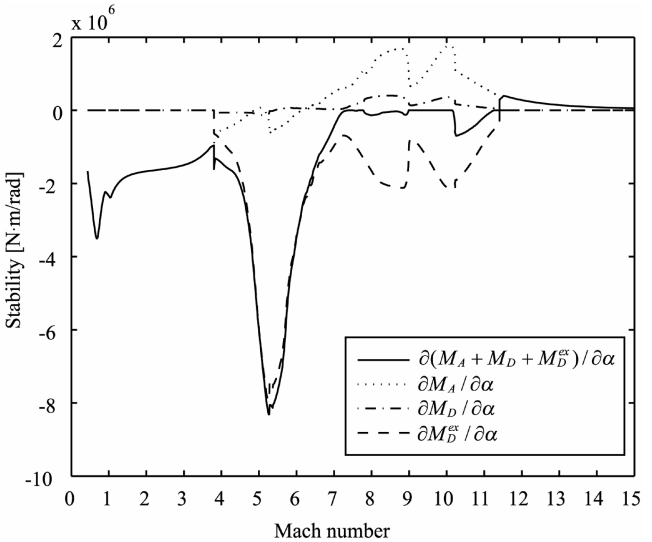

Fig. 11 Histories of stability characteristics with respect to flight Mach number (case 3).

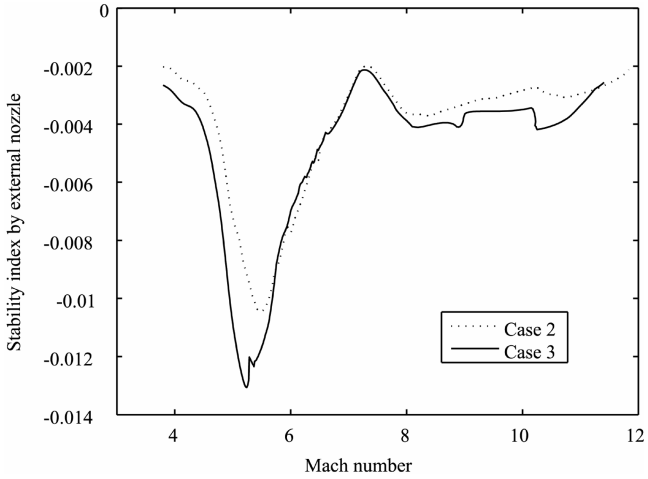

Fig. 12 Histories of stability index with respect to flight Mach number.

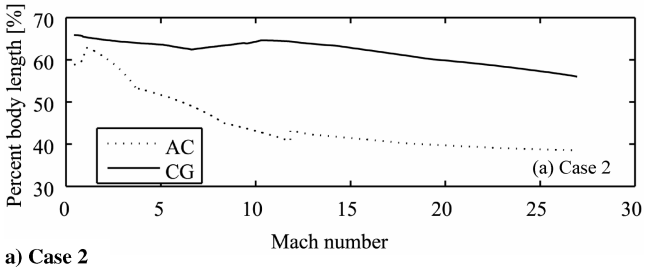

a) Case 2

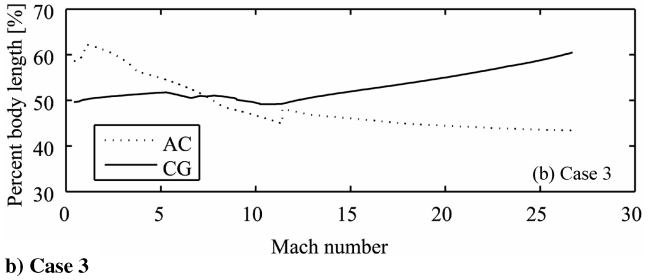

b) Case 3

Fig. 13 Histories of AC and CG with respect to flight Mach number.

nozzle, although it is still dependent on H, $\tilde{M}$, and $(\theta_f + \alpha)$. Figure 12 shows the values of $C^{\text{ex}}_{m\alpha}$ in cases 2 and 3. As can be seen in this figure, $C^{\text{ex}}_{m\alpha}$ in case 3 is almost the same or somewhat smaller than that in case 2, despite its larger θ_b. Thus, a large θ_b appeared to be preferred in case 3 so as to reduce the base drag while maintaining the stability enhancement effect.

Figure 13 shows the histories of the AC (excluding the engine effect) and CG positions in cases 2 and 3. There are discontinuities at the starting point and the terminal point of the DME operation. This is because in the calculation of the AC position in this figure, the pressure coefficient of the external nozzle excluding the combustion gas effect was approximated as zero during the DME operation. In case 2, the AC position was in front of the CG position throughout the flight, i.e., the vehicle was unstable throughout the flight. On the other hand, in case 3, the airframe of the vehicle was inherently stable up to around $\tilde{M} = 7$ and unstable thereafter. Nevertheless, the total stability was sustained by the external nozzle effect, as mentioned previously. The takeoff CG position in case 3 was located substantially forward than that in case 2 so as to attain a sufficient static margin, and it shifted rearward as the vehicle was accelerated. Moreover, it can be seen that the shift range of the AC position in case 3 was smaller than that in case 2.

V. Conclusions

An MDO problem of an SSTO space plane was formulated and solved in this study. The analysis model covered the rigid body characteristics such as trim and stability as well as the airframe-engine integration design. Using the all-at-once-based MDO approach, which incorporates sparse nonlinear programming and metamodeling, the design of the vehicle and its flight trajectory in 1) a trim-and-stability-unconstrained case, 2) a trim-constrained case, and 3) a trim- and stability-constrained case were successfully optimized.

The tradeoffs between the propulsion performance and the airframe geometry favorable for the rigid body characteristics (i.e., trim and stability) were observed. In particular, the trim- and stability-constrained solution had a large delta wing, shrinking forebody, and small external nozzle. In addition, the stability enhancement effect by the external nozzle was exploited in the optimal flight trajectory of the trim- and stability-constrained case. Moreover, the optimal trajectory appeared to be determined on the basis of the tradeoff between the structural weight and the propulsion performances.

Acknowledgment

This study was supported by a grant from the Japan Society of the Promotion of Science.

References

[1] Rowell, L. F., Braun, R. D., Olds, J. R., and Unal, R., "Multidisciplinary Conceptual Design Optimization of Space Transportation Systems," *Journal of Aircraft*, Vol. 36, No. 1, 1999, pp. 218–226.

[2] Braun, R. D., Moore, A. A., and Kroo, I. M., "Collaborative Approach to Launch Vehicle Design," *Journal of Spacecraft and Rockets*, Vol. 34, No. 4, 1997, pp. 478–486.

[3] Tartabini, P. V., Wurster, K. E., Korte, J. J., and Lepsch, R. A., "Multidisciplinary Analysis of a Lifting Body Launch Vehicle," *Journal of Spacecraft and Rockets*, Vol. 39, No. 5, 2002, pp. 788–795.

[4] Sobieszczanski-Sobieski, J., and Haftka, R. T., "Multidisciplinary Aerospace Design Optimization: Survey of Recent Developments," AIAA Paper 96-0711, 1996.

[5] Heiser, W. H., Pratt, D. T., Daley, D. H., and Mehta, U. B., *Hypersonic Airbreathing Propulsion*, AIAA,Washington, D.C., 1994, pp. 24–26.

[6] Yokoyama, N., "Multidisciplinary Optimization of Space Plane Modeled as Rigid Body," *Proceedings of the ICAS* [CD-ROM], International Congress on Aeronautical Sciences, 2004, pp. 172.1–172.10.

[7] Cramer, E. J., Dennis, J. E., Frank, P. D., Lewis, R. M., and Shubin, G. R., "Problem Formulation for Multidisciplinary Optimization," *SIAM Journal on Optimization*, Vol. 4, No. 4, 1994, pp. 754–776.

[8] Sobieszczanski-Sobieski, J., Agte, J. S., and Sandusky, R. R., Jr., "Bi-Level Integrated System Synthesis (BLISS)," NASA TM 1998-208715, 1998.

[9] Balling, R. J., and Wilkinson, C. A., "Execution of Multidisciplinary Design Optimization Approaches on Common Test Problems," *AIAA Journal*, Vol. 35, No. 1, 1997, pp. 178–186.

[10] Heiser, W. H., Pratt, D. T., Daley, D. H., and Mehta, U. B., *Hypersonic Airbreathing Propulsion*, AIAA, Washington, D.C., 1994, pp. 334–370.

[11] Kanda, T., Kudo, K., Tani, K., and Kato, K., "Calculation of Dual-Mode Engine Performance," *Proceedings of the Asian Joint Conference on Propulsion and Power 2005* [CD-ROM], Asian Joint Conference on Propulsion and Power Paper AJCPP-A20402005.

[12] Epton, M. A., and Magnus, A. E., "PAN AIR: A Computer Program for Predicting Subsonic or Supersonic Linear Potential Flows About Arbitrary Configurations Using a Higher Order Panel Method," Vol. 1, Theory Document (Ver. 3.0), NASA CR-3251 (Revision 1), 1991.

[13] Pittman, J. L., "Application of Supersonic Linear Theory and Hypersonic Impact Methods to Three Nonslender Hypersonic Airplane Concepts at Mach Numbers from 1.10 to 2.86," NASA TP-1539, 1979.

[14] White, F. M., *Viscous Fluid Flow*, 2nd ed., McGraw–Hill, New York, 1991, pp. 550–551.

[15] Bonner, E., Clever, W., and Dunn, K., "Aerodynamic Preliminary Analysis System Part 1: Theory," NASA CR-182076, 1991, p. 58.

[16] Tanner, M., "Theories for Base Pressure in Incompressible Steady Base Flow," *Progress in Aerospace Sciences*, Vol. 34, Nos. 7–8, 1998, pp.423–480.

[17] Eaton, J. K., and Johnston, J. P., "Review of Research on Subsonic Turbulent Flow Reattachment," *AIAA Journal*, Vol. 19, No. 9, 1981, pp. 1093–1100.

[18] Roshko, A., and Thomke, G. J., "Observations of Turbulent Reattachment Behind an Axisymmetric Downstream-Facing Step in Supersonic Flow," *AIAA Journal*, Vol. 4, No. 6, 1966, pp. 975–980.
[19] Raymer, D. P., *Aircraft Design: A Conceptual Approach*, AIAA, 3rd ed., 1999, pp. 563–566.
[20] Harloff, G. J., and Berkowitz, B. M., "HASA: Hypersonic Aerospace Sizing Analysis for the Preliminary Design of Aerospace Vehicles," NASA CR-182226, 1988.
[21] Anon., New Energy and Industrial Technology Development Organization Rept. 0100101141-9, 1997 (in Japanese).
[22] Nakata, Y., Taura, S., Nakayama, T., and Nakagawa, N., "Advanced Integrated Modular Avionics," *Journal of the Japan Society for Aeronautical and Space Sciences*, Vol. 52, No. 607, 2004, pp. 2–9 (in Japanese).
[23] Glatt, C. R., "WAATS: A Computer Program for Weights Analysis of Advanced Transportation Systems," NASA CR-2420, 1974.
[24] Sacks, J., Welch, W. J., Mitchell, T. J., and Wynn, H. P., "Design and Analysis of Computer Experiments," *Statistical Science*, Vol. 4, No. 4, 1989, pp. 409–435.
[25] Powell, M. J. D., "Radial Basis Functions for Multivariate Interpolation: A Review," *Algorithms for Approximation*, Edited by Mason, J. C., and Cox, M. G., Oxford, London, 1987, pp. 143–167.
[26] Chen, S., Cowan, C. F. N., and Grant, P. M., "Orthogonal Least Squares Algorithm for Radial Basis Function Networks," *IEEE Transactions on Neural Networks*, Vol. 2, No. 2, 1991, pp. 302–309.
[27] Yang, R. L., "Convergence of the Simulated Annealing Algorithm for Continuous Global Optimization," *Journal of Optimization Theory and Applications*, Vol. 104, No. 3, 2000, pp. 691–716.
[28] Yokoyama, N., Suzuki, S., and Tsuchiya, T., "Construction and Evaluation of RBF Network Approximation for Space Plane Aerodynamics," *Proceedings of the JSASS 41st Aircraft Symposium*, Paper No. IS17-11, 2003.
[29] Morris, M. D., and Mitchell, T. J., "Exploratory Designs for Computational Experiments," *Journal of Statistical Planning and Inference*, Vol. 43, No. 3, 1995, pp. 381–402.
[30] Betts, J. T., *Practical Methods for Optimal Control Using Nonlinear Programming*, 1st ed., Society for Industrial and Applied Mathematics (SIAM), Philadelphia, 2001.
[31] Brauer, G. L., Cornick, D. E., and Stevenson, R., "Capabilities and Applications of the Program to Optimize Simulated Trajectories (POST)," NASA CR-2770, 1977.
[32] Yokoyama, N., Suzuki, S., and Tsuchiya, T., "Convergence Acceleration of Direct Trajectory Optimization Using Novel Hessian Calculation Methods," *Journal of Optimization Theory and Applications* (accepted for publication).

J. Korte
Associate Editor